Atmos. Chem. Phys. Discuss., 11, 1–44, 2011
www.atmos-chem-phys-discuss.net/11/1/2011/
doi:10.5194/acpd-11-1-2011

Atmospheric Chemistry and Physics Discussions

Lagrangian coherent structures in tropical cyclone intensification

B. Rutherford[1], **G. Dangelmayr**[2], **and M. T. Montgomery**[1]

[1]Naval Postgraduate School, Monterey, CA, USA
[2]Department of Mathematics, Colorado State University, Fort Collins, CO, USA

Received: 23 March 2011 – Accepted: 21 September 2011 – Published:

Correspondence to: B. Rutherford (bdruther@nps.edu)

Published by Copernicus Publications on behalf of the European Geosciences Union.

Report Documentation Page

Form Approved
OMB No. 0704-0188

1. REPORT DATE	2. REPORT TYPE	3. DATES COVERED
MAR 2011		**00-00-2011 to 00-00-2011**

4. TITLE AND SUBTITLE	5a. CONTRACT NUMBER
Lagrangian coherent structures in tropical cyclone intensification	5b. GRANT NUMBER
	5c. PROGRAM ELEMENT NUMBER
6. AUTHOR(S)	5d. PROJECT NUMBER
	5e. TASK NUMBER
	5f. WORK UNIT NUMBER
7. PERFORMING ORGANIZATION NAME(S) AND ADDRESS(ES) **Naval Postgraduate School,Department of Meteorology,Monterey,CA,93943**	8. PERFORMING ORGANIZATION REPORT NUMBER
9. SPONSORING/MONITORING AGENCY NAME(S) AND ADDRESS(ES)	10. SPONSOR/MONITOR'S ACRONYM(S)
	11. SPONSOR/MONITOR'S REPORT NUMBER(S)

12. DISTRIBUTION/AVAILABILITY STATEMENT

Approved for public release; distribution unlimited

13. SUPPLEMENTARY NOTES

14. ABSTRACT

Recent work has suggested that tropical cyclones intensify via a pathway of rotating deep moist convection in the presence of enhanced fluxes of moisture from the ocean. The rotating deep convective structures possessing enhanced cyclonic vorticity within their cores have 5 been dubbed Vortical Hot Towers (VHTs). In general, the interaction between VHTs and the system-scale vortex, as well as the corresponding evolution of equivalent potential temperature !e that modulates the VHT activity, is a complex problem in moist helical turbulence. To better understand the structural aspects of the three-dimensional intensification 10 process, a Lagrangian perspective is explored that focuses on the localized stirring around VHTs and their vortical remnants, as well as the evolution and stirring of !e. Recently developed finite-time Lagrangian methods are limited in the three-dimensional turbulence and shear associated with the VHTs. In this paper, new Lagrangian techniques developed for three-dimensional velocity fields are summarized and we apply 15 these techniques to study VHT and !e phenomenology. Our primary findings are that VHTs are coherent Lagrangian vortices that create a turbulent mixing environment. Associated with the VHTs are hyperbolic structures that modulate the aggregation of VHTs and their vortical remnants. Although the azimuthally-averaged inflow is responsible for the inward advection of boundary layer 20 !e, the Lagrangian coherent structures are found to modulate the convection emanating from the boundary layer by stirring !e along organized attracting boundaries. Extensions of boundary layer coherent structures grow above the boundary layer during episodes of convection are responsible for organizing the remnants of the convective vortices. These hyperbolic structures form initially as boundaries between VHTs, but 25 persist above the boundary layer and outlive the VHTs to eventually form the primary eyewall as the vortex attains maturity.

15. SUBJECT TERMS

16. SECURITY CLASSIFICATION OF:			17. LIMITATION OF ABSTRACT	18. NUMBER OF PAGES	19a. NAME OF RESPONSIBLE PERSON
a. REPORT **unclassified**	b. ABSTRACT **unclassified**	c. THIS PAGE **unclassified**	**Same as Report (SAR)**	**44**	

Standard Form 298 (Rev. 8-98)
Prescribed by ANSI Std Z39-18

Abstract

Recent work has suggested that tropical cyclones intensify via a pathway of rotating deep moist convection in the presence of enhanced fluxes of moisture from the ocean. The rotating deep convective structures possessing enhanced cyclonic vorticity within their cores have been dubbed Vortical Hot Towers (VHTs). In general, the interaction between VHTs and the system-scale vortex, as well as the corresponding evolution of equivalent potential temperature θ_e that modulates the VHT activity, is a complex problem in moist helical turbulence.

To better understand the structural aspects of the three-dimensional intensification process, a Lagrangian perspective is explored that focuses on the localized stirring around VHTs and their vortical remnants, as well as the evolution and stirring of θ_e. Recently developed finite-time Lagrangian methods are limited in the three-dimensional turbulence and shear associated with the VHTs. In this paper, new Lagrangian techniques developed for three-dimensional velocity fields are summarized and we apply these techniques to study VHT and θ_e phenomenology.

Our primary findings are that VHTs are coherent Lagrangian vortices that create a turbulent mixing environment. Associated with the VHTs are hyperbolic structures that modulate the aggregation of VHTs and their vortical remnants. Although the azimuthally-averaged inflow is responsible for the inward advection of boundary layer θ_e, the Lagrangian coherent structures are found to modulate the convection emanating from the boundary layer by stirring θ_e along organized attracting boundaries. Extensions of boundary layer coherent structures grow above the boundary layer during episodes of convection are responsible for organizing the remnants of the convective vortices. These hyperbolic structures form initially as boundaries between VHTs, but persist above the boundary layer and outlive the VHTs to eventually form the primary eyewall as the vortex attains maturity.

ACPD
11, 1–44, 2011

1 Introduction

1.1 The turbulent intensification problem

1.1.1 VHT definition and their local dynamics

Observations show that tropical cyclones are highly asymmetric during their intensification phase. Once mature, only the most intense storms exhibit a strong degree of axial symmetry and even then, only in their inner-core region. Observations show also that intensifying storms are accompanied by bursts of convection, which one may surmise possess significant local buoyancy. When buoyant convection occurs in an environment of non-zero vertical vorticity, updrafts will amplify the vorticity by the process of vortex-tube stretching. There is growing evidence that convective bursts in pre-depression disturbances and tropical depression-strength storms do generate localized cyclonic vorticity anomalies in the lower troposphere whose magnitude exceeds that of the local environment by 1–2 orders of magnitude (Reasor et al., 2005; Sippel et al., 2006; Bell and Montgomery, 2010; Raymond and Lopez-Carrillo, 2010). The vertical convective structures that contribute to the stretching of cyclonic vertical vorticity in the low- to mid-troposphere will be hereafter referred to as vortical hot towers (or VHTs) (Hendricks et al., 2004; Dunkerton et al., 2009). Observations and numerical modeling studies suggest that VHTs typically have convective lifetimes on the order of 1 hour. Though the lifetime of VHTs is short, the amplified vorticity left behind may last much longer and contribute to the aggregation and upscale growth of the emerging cyclonic hurricane.

VHTs are a manifestation of convective instability, generated by moisture fluxes at the air-sea interface, in a rotating environment. Moisture fluxes enhance the moist entropy of the boundary layer above ambient values in the absence of convective- or meso-scale downdrafts, which import low moist entropy from aloft into the boundary layer. The local buoyancy required to support the VHTs is provided by the latent heat of condensation for moist air parcels originating in the atmospheric boundary layer.

ACPD
11, 1–44, 2011

It is only when a boundary layer parcel is lifted vertically (while conserving its moist entropy) to the so-called "level of free convection," that the parcel will acquire positive buoyancy to accelerate the updraft vertically and stretch vertical vortex tubes. The vertical buoyancy force per unit mass is proportional to the difference between the parcel's virtual temperature and that of its immediate environment. For convenience, the entropy of moist air is often expressed using the variable of equivalent potential temperature (θ_e) (Holton, 2004)[1].

The horizontal length scale of VHTs is on the order of 10 km and is thought to be associated with a (nonlinear) convective plume scale (Siggia, 1994), in contrast to the most unstable horizontal length scale (1 km or less) that arises in a linearized stability analysis of the moist tropical atmosphere (Lilly, 1960; Emanuel et al., 1994). As discussed in the foregoing paragraph, VHTs feed on heightened θ_e in the boundary layer. Because of their vortical properties, VHTs contribute to the stirring of θ_e anomalies in the boundary layer through high strain. The precipitation-driven downdrafts that accompany the VHTs in sub-saturated air import low θ_e from the middle troposphere into the boundary layer. Both of these processes create an environment less favorable for future convective episodes until the boundary layer θ_e recovers through the air-sea interaction process to a sufficient degree (Nguyen et al., 2010). The spatial distribution of boundary layer θ_e is therefore an integral component of the VHT dynamics and the spin-up of the system-scale circulation.

[1]For reference, the connection between the moist entropy (s) and θ_e is $s = c_p \ln(\theta_e)$, where c_p is the specific heat of dry air at constant pressure. For moist-saturated conditions, θ_e is adequately approximated by the quantity $\theta \exp(qL_v/c_pT)$ where $\theta = T(p_0/p)^{(R/c_p)}$ is the "dry" potential temperature, T is thermodynamic temperature, q is the mixing ratio of moist air (expressed in grams of water vapor per kilogram of dry air), p is air pressure, p_0 is a reference air pressure (1000 mb), R is the (ideal) gas constant for dry air and L_v is the latent heat of condensation. A more precise representation of θ_e for non-saturated and saturated conditions that includes the virtual temperature effect is given by Bolton (1980) and the Bolton formulation is employed for all θ_e calculations herein.

ACPD
11, 1–44, 2011

1.1.2 Role of VHTs in the spin up of the mean circulation

The role of VHTs in the intensification of the larger-scale vortex circulation has been the subject of recent numerical and theoretical investigations, (Hendricks et al., 2004; Montgomery et al., 2006; Nguyen et al., 2008; Shin and Smith, 2008; Nguyen et al., 2010; Montgomery et al., 2010; Fang and Zhang, 2010; Levina and Montgomery, 2010). From a mean-field viewpoint associated with an azimuthal average around the system center of circulation, VHTs have been implicated in two mechanisms for spinning up the mean vortex (Smith et al., 2009; Montgomery and Smith, 2011):

– The first mechanism is associated with the radial convergence of absolute angular momentum *above the boundary layer* in conjunction with its conservation [2]. The convergence of absolute angular momentum is produced by a system-scale radial gradient of a positive heating rate associated with the VHTs in the presence of enhanced surface moisture fluxes from the underlying ocean[3]. This mechanism has been articulated previously by many authors (e.g., Willoughby (1979); Schubert and Hack (1982)). It explains why the vortex expands in size (Smith et al., 2009) and may be interpreted in terms of balance dynamics (Bui et al., 2009), wherein

[2]The absolute angular momentum, $M = rv + 1/2fr^2$, is the sum of the planetary angular momentum taken about the storm's rotation axis and the relative angular momentum of the storm's tangential circulation. Here, r denotes radius from the system circulation center, f denotes the Coriolis parameter ($2\Omega\sin(\phi)$, where ϕ is latitude) and v denotes the azimuthally-averaged tangential velocity field, defined relative to the system center.

[3]The heating rate refers to the material derivative of the dry potential temperature, θ, defined in the previous footnote (see also Holton, 2004). Unlike the moist thermodynamic viewpoint discussed in the foregoing subsection in which moist air parcels lifted from the boundary layer rise along moist-adiabats materially conserving their moist entropy (and θ_e), in the alternative dry-thermodynamic viewpoint the latent heat that is liberated during the condensation process appears as a forcing term in the thermodynamical equation for θ. These two descriptions are complementary.

ACPD
11, 1–44, 2011

the azimuthal mean flow is well approximated by gradient wind and hydrostatic balance [4].

– The second mechanism is associated with radial convergence of absolute angular momentum *within the boundary layer* and becomes important in the inner-core region of the developing storm. Although absolute angular momentum is not materially conserved in the boundary layer, large wind speeds can be achieved if the radial inflow is sufficiently large to bring the air parcels to small radii with minimal loss of angular momentum. While coupled to the interior flow via the radial pressure gradient at the top of the boundary layer, and still requiring convectively-induced inflow above the boundary layer to increase the radial pressure gradient there, this spin-up pathway is tied to the dynamics of the boundary layer where the flow is not in gradient wind balance over a substantial radial span (Montgomery and Smith, 2011).

1.1.3 Motivation of this study

The two-stage model of tropical cyclone intensification proposed by Smith et al. (2009) is thus one that incorporates both the dynamics and thermodynamics of VHTs and their collective effects. In general, the interaction between VHTs and the system-scale vortex, as well as the corresponding evolution of θ_e, is a complex problem in moist helical turbulence [5] (Levina and Montgomery, 2010). To better understand the structural aspects of the intensification process, a Lagrangian perspective is adopted here for studying the localized stirring around VHTs and their vortical remnants, as well as the evolution and stirring of θ_e. One of the goals of this study is to understand further the system-scale implications of stirring and mixing processes near VHTs and their respective mergers.

[4] See Chapter 3 of Holton (2004) for a definition of gradient and hydrostatic balance.

[5] Helicity is the scalar product between the vorticity and velocity vector fields.

ACPD
11, 1–44, 2011

Another property of the new model is the stochastic nature in the development and interaction of the VHTs, due to the turbulent nature of the flow. Recalling the rule that the predictability time generally scales with the eddy turnover time of the energy containing eddies, it would seem that meaningful forecasts of the lifecycle of an individual VHT (i.e., formation, growth, merger with neighboring VHTs, and decay) are futile beyond a one hour time scale. Therefore, information about the aggregate contribution of the stochastic turbulent structures would be expected to be obtained by eddy statictics (Weiss and Provenzale, 2008). On the other hand, it is well known that flow boundaries tend to be persistent, even in time-dependent flows, and knowledge of the location of these boundaries within a highly time-dependent flow may improve the localized predictability of the turbulent mixing processes. A second goal of this study is to examine the localized effects of persistent Lagrangian boundaries associated with the VHTs which protect and aggregate regions of vorticity and protect the enhanced θ_e anomalies that support VHTs.

1.2 Organization within the turbulence

Persistent boundaries allow a simplified viewpoint of organized transport, and in steady or weakly time-dependent flows are formed by the stable and unstable manifolds of a trajectory with saddle-type stability, see Ide et al. (2002); Malhotra and Wiggins (1999). Flow boundaries for time-dependent flows still share a relationship to the saddle-point geometry for steady flows as they are finite-time manifolds, but the boundaries exist only for finite times, and are limited to finite lengths. Though the flow near VHTs is turbulent, some flow boundaries near VHTs have lifetimes greater than that of the VHT, and provide pathways for stirring of vorticity. Since the boundaries can be visualized in a reference frame moving approximately at the speed of the Lagrangian boundary through the time-dependent flow, these finite-time flow boundaries represent a type of Lagrangian coherent structure (LCS).

ACPD
11, 1–44, 2011

1.2.1 LCS definition

Lagrangian coherent structures are generally defined as structures which maintain some particular property when advected by the flow. While the Lagrangian reference frame in most meteorological applications follows a coherent feature, the dynamical systems community has recently used the term Lagrangian for following particle trajectories in order to provide a more generalized frame independent view of transport in time-dependent flows (Wiggins, 2005; Haller and Yuan, 2000). Shadden (2006), offers a definition of LCSs commonly accepted in the dynamical systems community as "ridges [6] of a Lagrangian scalar field." While VHTs are LCSs in the sense of the meteorological definition, their Lagrangian properties in the sense of the latter definition have not been studied extensively. To avoid confusion, the use of the term LCS will refer hereafter to a ridge of a Lagrangian scalar field, and will not be used to refer to a VHT.

Of particular interest for studying mixing are those LCSs which serve as the finite-time analogs of stable and unstable manifolds. Forward time integration yields repelling LCSs while backward time integration yields attracting LCSs, which are the finite-time analogs to stable and unstable manifolds, respectively. Attracting LCSs attract and then stretch a tracer blob, while repelling LCSs split a tracer blob that initially straddles the LCS (Haller and Yuan, 2000).

Table 1. Summary of the kinematic characteristics of LCSs.

manifold	LCS	integration time	effect on tracers
unstable	attracting	backward	stretching
stable	repelling	forward	splitting

[6] Ridges of a scalar field are curves which are locally maximal and the orientation of the curve is everywhere orthogonal to the gradient of the scalar field.

ACPD
11, 1–44, 2011

1.2.2 Finite-time Lagrangian methods

Locating LCSs in 3-D time-dependent flows is challenging, but is aided by a new class of techniques that have been developed in the past decade. The methods from dynamical systems theory allow for the detection of LCSs in flows with general time-dependence. Haller and coauthors (Haller and Poje, 1997; Haller and Yuan, 2000; Haller, 2000) proposed finite-time Lyapunov exponents (FTLE's) as a method for measuring trajectory separation, and defined LCSs as maximal ridges of FTLE fields. The method of FTLE's was shown to be robust under approximation errors of the velocity fields (Haller, 2002), and has been applied to a variety of fluid flows. Applications to atmospheric flows have been more limited, though several studies have ventured into this area. In Sapsis and Haller (2009), Rutherford et al. (2010b), and Rutherford et al. (2010a), FTLE's have been applied to tropical cyclones, and in Tang et al. (2010), FTLE's are used in a study of the subtropical jetstream.

Though FTLE's easily locate LCSs in time-dependent flows, they do not differentiate between hyperbolicity and shear effectively, and therefore would appear to have limited usefulness in flows with strong shear, such as the inner core region of an intensifying tropical cyclone. A method of separating hyperbolicity from shear was proposed by Haller and Iacono (2003), and was applied by Rutherford et al. (2010b) to detect LCSs in the presence of large-scale shear. The LCSs found were not manifolds, since they move with the dominant vortex Rossby wave structure, a propogating feature that is not simply the result of advection by the flow, but were shown to be robust across time, and were shown to influence the systematic radial transport of fluid particles within the evolving vortex.

The method of separating shear in two-dimensional flows was extended to 3-D in Rutherford and Dangelmayr (2010). The method was used to compute the Lagrangian boundary separating the eye and eyewall during a mature TC simulation. That study introduced a new view on 3-D flow separation by decomposing the growth

ACPD
11, 1–44, 2011

of material elements into several hyperbolic and shear components. Additionally, the hyperbolic fields converged faster than FTLE's and the field associated closely with the horizontal plane eliminated the need for rescaling vertical motions due to the small vertical:horizontal aspect ratio that typifies a tropical cyclone vortex. A specific choice of coordinates adapted to the helical trajectory motion made the approach of Rutherford and Dangelmayr (2010) more computationally efficient. Whereas the VHT interaction is clearly more complex than the evolution of a single mature hurricane vortex, the coordinate system proposed by Rutherford and Dangelmayr (2010) nonetheless resolves LCSs under shorter time-scales. We note that other studies (Truesdell, 1954; Saffman, 1981; Provenzale, 1999; Prieto et al., 2003; Shadden et al., 2006) have investigated the interaction between and entrainment of particles by vortices using different methods.

In this study, we apply the methods of Rutherford and Dangelmayr (2010) to a 3-D intensifying tropical cyclone, and examine the LCSs associated with VHTs. We show that while the VHTs are themselves a type of LCS, vertically coherent hyperbolic LCSs separating the VHTs are shown to control the organization of VHTs and their vortical remnants, and would thus appear to be important elements of the three-dimensional intensification process. Moreover, the hyperbolic LCSs cannot be isolated by the field of FTLE's even when only considering the two-dimensional flow. Our study shows also that the length of the hyperbolic LCSs is an important factor in VHT interaction, as the VHTs interact when the LCSs are long enough to span between them. The structures we find are long enough to span multiple VHTs, and may contribute to the upscale organization proposed by Montgomery et al. (2006), Nguyen et al. (2008), and Shin and Smith (2008).

1.2.3 Outline

The outline of the remainder of this paper is as follows. Section 2 provides an overview of the coordinate system and the Lagrangian methods used in this 3-D study. In Sect. 3, the meteorological model from which the velocity data are calculated is described, along with numerical details regarding trajectory calculations. The reader interested

ACPD
11, 1–44, 2011

primarily in the key findings may skip to Sect. 4 where the main results are presented. The structures revealed by the Lagrangian fields indicate two primary roles of LCSs: the modulation of rotating deep moist convection by stirring θ_e along organized attracting boundaries; and the organization of cyclonic vertical vorticity above the boundary layer, which is stretched along coherent structure boundaries in the boundary layer to form the primary eyewall. We conclude, in Sect. 5, with further remarks on the relation between Lagrangian coherent structures and VHTs, and provide an outlook on future studies stimulated by the results of this paper.

2 Mathematical preliminaries

We denote all vector quantities using boldface, and all matrices in capitalized regular font. An asterik refers to a transposed vector or matrix.

The Lagrangian trajectory based approaches in previous studies (Haller and Yuan, 2000; Haller, 2002; Shadden et al., 2005; Rutherford and Dangelmayr, 2010) utilize particle trajectories $\mathbf{x}(t)$, which evolve according to the flow map after time T,

$$\mathbf{x}(t_0) \rightarrow \mathbf{x}(t_0, t_0 + T). \quad (1)$$

The methods detect LCSs by measuring Lagrangian stretching along trajectories through the linearized growth of perturbations, which grow according to the variational equation

$$\dot{\boldsymbol{\xi}} = \nabla \mathbf{u}(\mathbf{x}(t), t)\boldsymbol{\xi}, \quad (2)$$

where $\mathbf{u}(\mathbf{x}, t)$ is, in this paper, a 3-D velocity field as in Rutherford and Dangelmayr (2010). Finite-time Lyapunov exponents (FTLE's) and similar metrics measure the linearized growth as the separation of nearby trajectories, and provide scalar fields which show LCSs corresponding to stable and unstable manifolds as ridges. Computing the FTLE forward ($T > 0$) and backward ($T < 0$) in time allows detection of forward time repelling and attracting material lines, respectively.

ACPD
11, 1–44, 2011

While FTLE's are an efficient measure of trajectory separation, they do not differentiate between hyperbolicity and shear. The study of LCSs in sheared flow for a 2-D nondivergent barotropic vortex (Rutherford et al., 2010b) showed that FTLE's were not well suited when the radial velocity terms were dominated by the radial derivative of angular velocity $\partial\omega/\partial r$. For the experiment used in this study, there is sufficient radial flow so that FTLE's are a suitable diagnostic in some cases. In regions with strong horizontal shear, the orthogonal growth rate of small perturbations caused by persistent strain can still be isolated by solutions of (2) as discussed in the following.

The Lagrangian velocity direction is given by the unit tangent vector

$$\mathbf{t} = \frac{\mathbf{u}}{|\mathbf{u}|}, \tag{3}$$

evaluated along trajectories. A moving frame of reference for (2) is introduced along a trajectory by setting

$$\boldsymbol{\xi} = T(\mathbf{x}(t),t)\boldsymbol{\eta}, \tag{4}$$

where the columns of T are the orthogonal unit vectors $\mathbf{t},\mathbf{n},\mathbf{b}$,

$$T(\mathbf{x},t) = [\mathbf{t}(\mathbf{x},t),\mathbf{n}(\mathbf{x},t),\mathbf{b}(\mathbf{x},t)]. \tag{5}$$

The transformed system for $\boldsymbol{\eta}$ has the form

$$\dot{\boldsymbol{\eta}} = [A(\mathbf{x}(t),t) + B(\mathbf{x}(t),t)]\boldsymbol{\eta}, \tag{6}$$

where

$$A(\mathbf{x},t) = T^*(\nabla\mathbf{u})T - T^*(T_{\mathbf{x}}\dot{\mathbf{x}}) \tag{7}$$

with

$$T_{\mathbf{x}}\dot{\mathbf{x}} = \left[(\nabla\mathbf{u})\mathbf{t} - [\mathbf{t}^*(\nabla\mathbf{u})\mathbf{t}]\mathbf{t}, (\nabla\mathbf{n})\mathbf{u}, (\nabla\mathbf{b})\mathbf{u}\right],$$

ACPD
11, 1–44, 2011

and $B(\mathbf{x},t) = -[\mathbf{b}_1, T^*\mathbf{n}_t, T^*\mathbf{b}_t]$ with $\mathbf{b}_1 = (1/|\mathbf{u}|)[0, \mathbf{n}^*\mathbf{u}_t, \mathbf{b}^*\mathbf{u}_t]^*$ contains all terms of the transformed matrix that depend on the time derivatives of $\mathbf{u}, \mathbf{n}, \mathbf{b}$ (indicated by the subscript t), thus B vanishes in the case of steady velocity fields,

$$\dot{\boldsymbol{\eta}} = A(\mathbf{x}(t),t)\boldsymbol{\eta}. \tag{8}$$

As in previous studies (Rutherford and Dangelmayr, 2010; Rutherford et al., 2010b), we assume that the time-variation of fluid velocities along trajectories is small and can be neglected for short integration times. Thus we use Eq. (8) to approximate finite-time solutions of the transformed variational system. Combining the two terms of which A is composed in Eq. (7) yields $A = [\mathbf{a}_1, T^*\mathbf{a}_2, T^*\mathbf{a}_3]$, where

$$\mathbf{a}_1 = [\mathbf{t}^*(\nabla\mathbf{u})\mathbf{t}, 0, 0]^*,$$
$$\mathbf{a}_2 = (\nabla\mathbf{u})\mathbf{n} - (\nabla\mathbf{n})\mathbf{u},$$
$$\mathbf{a}_3 = (\nabla\mathbf{u})\mathbf{b} - (\nabla\mathbf{b})\mathbf{u}.$$

2.1 Transformation to upper triangular form and solution of the variational system

In contrast to the 2-D case of Rutherford et al. (2010b), the matrix A is not upper triangular. To obtain upper triangular form we apply a time-dependent orthogonal transformation in the normal plane. The normal plane component, $\boldsymbol{\eta}^\perp = (\eta_2, \eta_3)^*$, satisfies $\dot{\boldsymbol{\eta}}^\perp = A^\perp\boldsymbol{\eta}$ with

$$A^\perp = \begin{pmatrix} A_{22} & A_{23} \\ A_{32} & A_{33} \end{pmatrix}. \tag{9}$$

Let $\phi(t)$ be a solution to the differential equation

$$\dot{\phi} = \frac{1}{2}(A_{33} - A_{22})\sin 2\phi + A_{23}\sin^2\phi - A_{32}\cos^2\phi, \tag{10}$$

ACPD
11, 1–44, 2011

and $R(\phi)$ the rotation matrix

$$R(\phi) = \begin{pmatrix} \cos\phi & \sin\phi \\ -\sin\phi & \cos\phi \end{pmatrix}. \tag{11}$$

The transformation $\boldsymbol{\eta}^{\perp} = R(\phi(t))\widetilde{\boldsymbol{\eta}}^{\perp}$ transforms the normal plane system to

$$\dot{\widetilde{\boldsymbol{\eta}}}^{\perp} = \widetilde{A}^{\perp}\widetilde{\boldsymbol{\eta}}^{\perp}, \tag{12}$$

where $\widetilde{A}^{\perp}$ is upper triangular. Thus, dropping the tilde, we may assume that A in Eq. (8) has the form

$$A(\mathbf{x}(t),t) = \begin{pmatrix} A_{11} & A_{12} & A_{13} \\ 0 & A_{22} & A_{23} \\ 0 & 0 & A_{33} \end{pmatrix}, \tag{13}$$

and the transformed variational system can be solved by direct integration. The fundamental matrix whose columns are linearly independent solutions for the system (8) with A given by Eq. (13) is found by direct integration as

$$\Psi(t,t_0) = \begin{pmatrix} \Psi_{11}(t,t_0) & \Psi_{12}(t,t_0) & \Psi_{13}(t,t_0) \\ 0 & \Psi_{22}(t,t_0) & \Psi_{23}(t,t_0) \\ 0 & 0 & \Psi_{33}(t,t_0) \end{pmatrix}, \tag{14}$$

where the diagonal elements can be written as

$$\Psi_{ii}(t,t_0) = \exp\Big(\int_{t_0}^{t} A_{ii}(\tau)\,d\tau\Big),$$

ACPD
11, 1–44, 2011

and the off-diagonal elements as

$$\begin{aligned}
\Psi_{12} &= \int_{t_0}^{t} \exp\left(\int_s^t A_{11}(\tau)d\tau\right) \\
&\quad \exp\left(\int_{t_0}^{s} A_{22}(\tau)d\tau\right) A_{12}(s)ds, \\
\Psi_{23} &= \int_{t_0}^{t} \exp\left(\int_s^t A_{22}(\tau)d\tau\right) \\
&\quad \exp\left(\int_{t_0}^{s} A_{33}(\tau)d\tau\right) A_{23}(s)ds, \\
\Psi_{13} &= \int_{t_0}^{t} \exp\left(\int_s^t A_{11}(\tau)\tau\right)\left[\Psi_{23}(s,t_0)A_{12}(s)\right. \\
&\quad \left. + \exp\left(\int_{t_0}^{s} A_{33}(\tau)d\tau\right) A_{13}(s)\right] ds.
\end{aligned} \tag{15}$$

For a 3-D hurricane flow, the particle motion in the eyewall can be described as helical, with rotational and vertical components.

Horizontally aligned normal vector

Numerical implementation of the TNB coordinate frame can be simplified by choosing **n** to be the outward normal vector

$$\mathbf{n} = \mathbf{u}_\mathrm{h}^{\perp}/|\mathbf{u}_\mathrm{h}|, \tag{16}$$

where $\mathbf{u}_\mathrm{h} = (u,v,0)^*$ is the horizontal component of the velocity, and $\mathbf{u}_\mathrm{h}^{\perp} = (-v,u,0)^*$. In this case the binormal is given by

$$\mathbf{b} = \frac{1}{|\mathbf{u}||\mathbf{u}_\mathrm{h}|}\left(-uw,-vw,|\mathbf{u}_\mathrm{h}|^2\right)^*, \tag{17}$$

and the entries A_{ij} with $i > 1$ in (13) become

$$A_{12} = \frac{1}{|\mathbf{u}||\mathbf{u}_\mathrm{h}|}\left\{(u^2-v^2)(u_y+v_x)+2uv(v_y-u_x)\right.$$

ACPD
11, 1–44, 2011

$$+uw(v_z+w_y)-vw(u_z+w_x)\Big\},$$

$$A_{13}=\frac{1}{|\mathbf{u}|^2|\mathbf{u}_h|}\Big\{(|\mathbf{u}_h|^2-w^2)\big(v(v_z+w_y)$$
$$+u(u_z+w_x)\big)-2w(u^2u_x+v^2v_y)$$
$$-2uvw(u_y+v_x)\Big\},$$

$$A_{22}=\frac{1}{|\mathbf{u}_h|^2}\Big\{u^2v_y+v^2u_x-uv(u_y+v_x)\Big\},$$

$$A_{23}=\frac{|\mathbf{u}|\left(uv_z-vu_z\right)}{|\mathbf{u}_h|^2},$$

$$A_{32}=\frac{1}{|\mathbf{u}||\mathbf{u}_h|^2}\Big\{2w\left(v^2v_x-u^2u_y+\right.$$
$$\left.uv(u_x-v_y)\right)+w^2(vu_z-uv_z)$$
$$+|\mathbf{u}_h|^2\left(uw_y-vw_x+w(u_y-v_x)\right)\Big\},$$

$$A_{33}=\frac{1}{|\mathbf{u}|^2|\mathbf{u}_h|^2}\Big\{w^2\left(u^2u_x+v^2v_y+uv(u_y+v_x)\right)$$
$$-|\mathbf{u}_h|^2w\left(u(u_z+w_x)+v(v_z+w_y)\right)$$
$$+|\mathbf{u}_h|^4w_z\Big\}.$$

For further mathematical details we refer to Rutherford and Dangelmayr (2010).

ACPD
11, 1–44, 2011

3 Model description and numerical implementation of Lagrangian fields

3.1 Setup

The model used to generate data for this study is the fifth generation Penn State/NCAR mesoscale model (MM5), Grell et al. (1995) and Dudhia (1993). The model run is a fully 3-D nonhydrostatic simulation of an idealized tropical cyclone on an f-plane. The model employs a bulk aerodynamic scheme for representing the fluxes of sensible heat, moisture, and momentum between the atmosphere and the ocean. The model calculations were initialized using a convectively neutral environment and an axisymmetric warm-core, cloud-free vortex with a maximum surface tangential velocity of 15 m s^{-1} at a radius of 135 km (Nguyen et al., 2008). The intensification of the vortex is highlighted in Fig. 1 by plotting the local maximum of horizontal wind speed as a function of time. The exact model data used in this study is taken from experiment 12 of Montgomery et al. (2009). The wind-speed dependence of the heat and moisture fluxes from the underlying ocean surface is retained in this experiment. Though the initial condition is axisymmetric, asymmetries develop quickly around 8 h in the form of near-columnar convective structures posessing strong cyclonic vorticity in their cores. As discussed in the Introduction, these structures are called VHTs. As the vortex intensifies, the number of VHTs progressively decreases as the vortex attains maturity. By the end of the rapid intensification period (approximately 60 h and onwards), no more than three VHTs are active around the circulation centre (not shown). In the mature phase, the evolution of the vortex core is characterized by an approximately axisymmetric circulation superimposed on which are small, but finite-amplitude vortex Rossby waves that propagate azimuthally, radially, and vertically on the mean potential vorticity gradient of the system-scale vortex (Bui et al., 2009), coupled to the to the boundary layer and convection (Wang, 2000; Chen and Yau, 2003; Smith et al., 2008). In this study we examine fields from times of $t = 0$ to 50 h during the main intensification phase.

The model run used in this study utilized four nested grids, and 3-D velocity data is taken only on the innermost 300 km square grid with $x - y$ grid spacing of 1.67 km.

ACPD
11, 1–44, 2011

Vertical coordinates are given on σ–levels, and vary in time, with an output time-step of 2 min. Trajectory integrations are performed using a fourth order Runge-Kutta scheme, on grids of evenly spaced points in a box of size 220 km by 220 km by 16 km in x, y, and z respectively, with horizontal grid-spacing of 1 km, and vertical grid-spacing of 250 m.

3.2 Time and length scales

The relationship between the time and length scales of VHTs and those of the LCSs near them drive our choice of integration time for the LCSs. A longer integration time resolves and lengthens LCSs. However, spurious structures and excessive filamentation may emerge for long integration times due to the time-dependence. A short integration time will not resolve as many LCSs, but will not show spurious structures and requires less computation time. Since the representative lifetime of a VHT is 1 h, we have chosen $T = 1$ h as the primary integration time. This choice limits mergers or splitting of the LCSs as the VHTs die, yet is still sufficiently long to reveal LCSs that span between the VHTs, including LCSs which are associated with vortical remnants and have a lifespan on the order of 10 hours. Our approach to understand time-dependent stirring is to consider LCSs which are well resolved under a short integration time and coherent across varying initial times. We note that the width of LCSs are often less than the width of the $x-y$ grid spacing, which shows that the existence of LCSs are dependent on model resolution. In fact, smaller trajectory grid-spacing yields finitely many additional LCSs which are at sub model grid-scale, while retaining the primary LCSs detected by coarser trajectory grids.

The initial time, t_0, is varied between 5 and 50 h, which captures the model time interval in which VHTs organize vorticity into a symmetric ring-like structure. The convention for Lagrangian fields is to define the Lagrangian field at the initial time of integration, t, since they are integrated quantities and incorporate velocities from the interval $(t, t+T)$. The Lagrangian fields at time t are compared to Eulerian fields at a fixed time t, so t

ACPD
11, 1–44, 2011

refers to both initial time of the Lagrangian fields and model output time of Eulerian fields.

During the evolution from 5 h to 50 h, the number of VHTs decrease as the storm intensifies, with the maximal tangential wind speed increasing from 15 m s^{-1} at 5 h to over 60 m s^{-1} at 50 h. The asymmetric stage begins at 8 h with modestly high θ_e in an 80 km ring (Fig. 2c), which, in conjunction with the frictional convergence in the boundary layer, induces convective instability and the formation of VHTs beginning just before 10 h coincident with the first sharp rise in intensity (Fig. 1). As the VHTs interact they comprise the bulk of the system scale radial gradient of latent heating. This heating gradient leads to a radial influx of vertical vorticity and θ_e acquired through the air-sea interaction process. An eye-like feature forms at approximately 40 h, Fig. 2e, with a ring of maximal cyclonic vorticity evident near 40 km radius and the highest θ_e located interior to this radius at approximately 30–35 km.

Recent work (Nguyen et al., 2010; Montgomery et al., 2009) indicates that the localized effects of the VHTs are (i) stirring of θ_e in the boundary layer, (ii) the consumption of convective available potential energy (Holton 2004) and restoration of convective stability, and (iii) the stirring of vorticity in the local environment. The convective component of a VHT subsides when either (i) the VHT has consumed all of the convective available potential energy in its immediate vicinity, and or (ii) vertical shear differentially advects the columnar structure disrupting the lifecycle.

In the next section, we will adopt the Lagrangian perspective by examining how LCSs influence the localized transport of vorticity and θ_e. LCSs will be shown to contribute to the fluid dynamics by (i) convergence in the boundary layer and inward movement of θ_e, (ii) turbulent updrafts due to the transport of heightened θ_e anomalies out of the boundary layer, and (iii) preferential location of vortical remnants above the boundary layer dictated by the presence of coherent structures which protect the vortices from regions of high strain. The LCSs' influence on the vortices continues with (iv) inward convergence of vorticity along attracting boundaries which leads to the formation of a primary eyewall.

ACPD
11, 1–44, 2011

3.3 LCSs

3.3.1 Lagrangian field computations

LCSs can be seen as maximal ridges of fixed-time Lagrangian scalar fields, and can be tracked over varying initial times. Attracting LCSs are found mainly along the boundaries of regions with high θ_e. Repelling LCSs guide VHTs toward the center of the LCS, and tend to preserve the VHT without stretching it. The FTLE field is computed on a trajectory grid, and due to the small vertical to horizontal aspect ratio of the model output domain, the inclusion of the vertical component in the computation of FTLE's reduces the resolution of ridges under a fixed integration time. By eliminating the vertical separation, the "planar" FTLE field is computed from the horizontal separation of a horizontal grid of trajectories which are allowed 3-D motion, and resolves ridges much faster than the 3-D FTLE field. Horizontal shear is computed as in Rutherford and Dangelmayr (2010) by the angle of rotation of the η_2 variable onto the η_1 variable subspace defined by $\arctan\varphi = \Psi_{12}/\Psi_{22}$, with values of φ near $\pi/2$ showing maximal shear.

3.3.2 Fixed-time Lagrangian fields

Though Lagrangian values are defined along any trajectory, and fields are computed on 3-D grids, we show the Lagrangian fields on z-levels for ease of visualization of the LCSs. To illustrate the spatial forms of these structures, we show in Figure 3 the planar FTLE, Ψ_{22}, and φ fields at $z = 1$ km and 10 h, along with zooms highlighting a particular structure to compare the Lagrangian fields. The FTLE maxima occur at any point of high separation, including shear lines surrounding vortices and hyperbolic lines, while the Ψ_{22} field isolates hyperbolic separation. We note that Ψ_{22} ridges are generally in regions of low shear between VHTs and do not enclose VHTs. We specifically refer to these LCSs as Ψ-LCSs to distinguish them from LCSs that are associated with FTLE's. The particular structure highlighted in the closeup views shows that the FTLE ridge encloses two rings of vorticity, and contains the connecting region between them.

ACPD
11, 1–44, 2011

The VHTs are in regions of high shear, so the FTLE ridge surrounding them does not have hyperbolic stability.

To relate the LCSs to vorticity and θ_e in both forward and backward time, the ridges of the Lagrangian fields are approximated by contours and are overlaid along with vorticity contours on θ_e fields. We show LCSs which are ridges that have Lagrangian values of over 80 % of the maximum Lagrangian values.

4 Lagrangian fields

4.1 Temporal evolution

The lifespan of most LCSs is approximately the same as the 1 h lifetime of VHTs since the merger or disappearance of VHTs alters the saddle-type geometry of the LCS and causes them to merge or split. Additionally, single LCSs between vortices may appear, disappear, or change stability type. Appearance or disappearance of an LCS generally occurs on the same time scale as VHTs, and is related to the merger of a pair of VHTs or the death of a VHT, and are not coincident with organized stirring. However, organization by the splitting and merger of LCSs or change in stability of a LCS may allow LCSs to overcome the high time-dependence and persist for much longer than 1 hour. The change in stability of an LCS may be impacted also by the existence of differential rotation associated with the horizontal swirling flow, Rutherford et al. (2010b). The difference in radial velocity between VHTs may prohibit the hyperbolic stability of the LCSs. Since LCSs that exist for short times are related to a single VHT, we primarily consider LCSs which last longer than the typical VHT.

4.2 Convection and vertical structure

Because of the rotation, convective vortices exhibit vertical coherence of Lagrangian fields as well as vorticity and θ_e. In Fig. 4, we show an example of Lagrangian fields and

ACPD
11, 1–44, 2011

vorticity overlaid on θ_e at levels of 40 m, 1 km, 4 km, and 7 km. Many pools of vorticity can be seen extending from the sea surface to heights of 7 km and higher, showing the vertical coherence associated with vortex tube stretching in a rotating environment. The pools of high θ_e are in similar planar locations as the vortices from the sea-surface to 4 km height, and to 7 km height in the smaller radius VHTs.

The local in, up and out trajectory motion associated with VHTs during a forward time integration adds uncertainty to the planar projection of the particles' final locations. Consequently, the deep convection associated with VHTs is typically seen in the FTLE field by a "tangle" of repelling LCSs, Fig. 4 (in red). The signature of deep convection in low-level FTLE fields can be seen by comparing the FTLE-fields at 1 km in Fig. 4b with the θ_e fields at 7 km in Fig. 4d. The figures show that θ_e at upper levels is coincident with high FTLE values at low levels. Moreover, the most intense convection is coincident with greater vertical coherence of the tangle, which suggests that trajectories remain entrained through convection. As an example, we show two specific vortices with different vertical characteristics marked A and B in Fig. 4. Vortex A has vertically coherent LCSs and is convectively active to 7 km. Vortex B has no LCSs at 4 km, and the coherence of vorticity and θ_e does not reach 4 km.

4.3 Azimuthal average

As a preliminary step in comparing the Lagrangian quantities, we show the radius-time portrayal of several diagnostics in Figure 2. The evolution of azimuthally averaged Lagrangian fields (FTLEs and Ψ_{22}) indicate that higher Lagrangian values are broadly coincident both radially and temporally with higher wind speeds, and higher θ_e. While the distribution of wind speed maxima is radially diffuse, the Lagrangian maxima are more localized. The radial location of Ψ_{22} maxima, are near the inner core vortex edge where vorticity is maximized, Fig. 2e and f, while FTLEs are large throughout the region of high radial shear, Fig. 2d. While vorticity mixes toward the origin, Ψ_{22} does not, as it is associated with the eyewall boundary. Comparing the vorticity fields and Ψ_{22} fields, (Fig. 5c and d), shows that while the maxima occur at similar radii, they

ACPD
11, 1–44, 2011

generally occur at different azimuths. As will be discussed in Sect. 4.6, the Ψ_{22} ridges will be suggested to be important for the merging of vortical remnants, and they tend to occur inside the radius of maximal tangential winds, even during the intensification phase, consistent with the findings of Rutherford and Dangelmayr (2010).

4.4 Vortex flow geometry

To help understand the movement and interaction of intense vortices in a turbulent flow, we present conceptual models to illustrate the planar geometry of a vortex or pair of vortices in relation to a nearby saddle point in Fig. 6.

4.4.1 Convergent vortex

Convection at the center of VHTs allows a 2-D conceptual representation of the 3-D vortex geometry by projecting the helical trajectories onto a 2-D slice, which is a convergent vortex or stable spiral. A convergent vortex in a 2-D slice near a saddle point exhibits the flow geometry shown in Fig. 6a, where a branch of the unstable manifold of the saddle spirals toward the center of the vortex. Material entering the vortex travels toward and then along the unstable manifold toward the vortex center. Despite the time-dependent nature of VHTs, the geometry may be preserved or partially preserved for finite times in the Lagrangian frame.

4.4.2 Vortex interactions

Vortex interaction occurs across all spatial scales during intensification, from dipoles of small VHTs with length scales of less than 10 km to the interaction of broad system-scale vortices. Kinematically, two convergent vortices are associated with a single saddle when the vortices are formed by separate unstable manifold branches of the saddle trajectory, with the manifolds enclosing the vortices in a figure-eight pattern, Fig. 6b. If the flow was slowly time-dependent the vortices would interact through the mechanism of lobe dynamics described by Ide et al. (2002). For a highly time-dependent flow, the

ACPD
11, 1–44, 2011

vortices still interact, but the interaction is dependent on the manifold geometry, the time-dependence, and the relative time-scales of the stable and unstable directions of the saddle. Time-dependence limits the lengths and existence times of LCSs, and does not allow the figure-eight pattern to completely form. The relative time-scales of stable and unstable processes have not been considered in other studies to our knowledge, but these time scales form the basis for a classification of finite-time vortex interactions. Here we classify the interaction of cyclonic vortices (VHTs or their remnants) into stable, unstable, or complete interaction based on the stability of LCSs between them.

Stable interaction

Stable vortex interaction as depicted in Fig. 6c occurs when the influence of the repelling LCS is greater than that of the attracting LCS. This situation is most often observed with vortical remnants of VHTs and Ψ-LCSs. A repelling Ψ-LCS appears between adjacent vortices while an attracting LCS does not appear. The flow direction for cyclonic vortices associated with the system-scale circulation dictates the connection of the LCS to be radially inward of the leading vortex and radially outward of the trailing vortex. The vortices move toward the center of the LCS, but do not mix since they remain separated by the LCS. Because of the general in, up and out circulation driven by the aggregate heating of the VHTs, the vortices at low-levels have a tendency to move radially inward in the absence of flow boundaries, and often merge after the LCS vanishes.

Unstable interaction

Unstable vortex interaction as depicted in Fig. 6d is the basic type of interaction for convergent vortices along attracting LCSs, which tend to horizontally stretch VHTs or their remnants. The formation of an attracting LCS between two adjacent VHTs forces the orientation to be opposite the case for stable vortex interaction. As the vortices are

ACPD
11, 1–44, 2011

attracted to the LCS, the vortex tends to be stretched toward the tail, forming vorticity strips. Unstable vortex interaction generally occurs on a time-scale similar to the VHT lifetime.

Hyperbolic noninteraction

Hyperbolic vortex noninteraction occurs over short times when both attracting and repelling LCSs are resolved between vortices. Since high time-dependence limits the length of the LCSs, the hyperbolic vortex noninteraction does not induce lobe dynamics, and lasts for at most a few hours. Vortices which remain separated by the LCSs can be drawn arbitrarily close without merging, in contrast to the results of Melander et al. (1988) for freely decaying turbulence.

An illustrative example of vortex interaction

A case of interacting vortices can be seen in Fig. 7 during the time period from 29 h to 31 h. At 29 h, there are initially 3 prominent vorticity pools in the lower troposphere, labelled A, B, and C in Fig. 8a which form part of a pentagonal structure. A saddle point located between vortex A and vortex B creates a separatrix which divides the vortices, as in Fig. 7b. Over the next hour, all the vorticity pools and LCSs travel together, and at 30.4 h, vortices A and B come very close, yet remain separated by the attracting LCS. The relationship between vortex B and vortex C is different, however, since they are separated by a single LCS (e.g., Fig. 7d) instead of a complete separatrix. Vortices B and C are not connected at 29 h, but a repelling LCS creates a separatrix by 29.8 h. These latter two vortices travel along the LCS and then merge just after 31 h, as the vortex C absorbs vortex B.

4.5 Stirring of θ_e in the boundary layer

Having examined the interaction of intense vortices, we now consider the enhancement and distribution of the source of fuel for the vortices. Surface fluxes of moisture increase

ACPD
11, 1–44, 2011

θ_e at the bottom of the boundary layer, and θ_e is drawn inward by the convergent circulation. In the absence of the import of dry air from aloft, θ_e increases on inflow trajectories. Alongside the system-scale convergence, the LCSs reveal preferential locations for the convergence of θ_e near the sea-surface, which subsequently leads to localized convection.

The evolution of boundary layer θ_e can be seen in Figs. 8 and 9 by time snapshots at 2 h intervals of θ_e along with vorticity contours and attracting and repelling coherent structures at the lowest model output of 40 m. A ring of high θ_e near the VHT locations is transformed to a pool of high θ_e in the center. At the same time, low θ_e from the center diminishes as it is either expelled outward or enhanced by moisture fluxes in regions of air-sea disequilibrium. While θ_e values increase radially inward, specific focal points of high θ_e are horizontally constrained by the LCSs, which primarily occur along θ_e gradients. Specific boundaries and θ_e pools can be tracked over the time interval shown. Many of the LCSs which at 20 h bound dry air in the center are still present at 30 h. These LCSs can be tracked over the time interval and, after reorganization, are still present at 30 h as a boundary to protect elevated θ_e air near the vortex center.

4.6 Organization of vortical remnants above the boundary layer

The boundary layer does not give a complete view of vortex interaction, since there are no hyperbolic repelling LCSs due to the strong convergence there. However, above the boundary layer, these structures are combined with attracting LCSs to form the boundaries that control vortex interaction there. We now examine the temporal evolution of the LCSs during the time period from 20–30 h at the top of the boundary layer. We see that while the VHTs and θ_e anomalies that support them create an environment of turbulent convection, the LCSs show an organized view of the inward transport of vortical remnants. Regions of "organized" mixing form LCSs which are longer lasting than other LCSs or individual VHTs.

These LCSs are associated with vortical remnants thatremain intact for much longer than the normal 1 h lifetime of a VHT, and grow to diameters of 30 km. These vortices

ACPD
11, 1–44, 2011

are involved in many organized mergers as described in Sect. 4.2 along persistent Ψ-LCSs.

In contrast, the turbulent regime shows strong filamentation, marked by numerous short, intertwined FTLE ridges. However, there are few repelling Ψ-LCSs. Turbulent regions have vortices with the strongest convection. The LCSs in turbulent regions are generally not coherent for longer than 1 h, and the VHTs in turbulent regions do not leave behind persistent remnants.

4.7 Evolution of preferred remnants

The roles of FTLE and Ψ_{22} fields above the boundary layer are contrasted by showing the evolution of FTLEs in Fig. 10 with the Ψ_{22} ridges in Fig. 11. Organized and turbulent regimes as defined above are approximately outlined by boxes, and labeled O and T respectively. At 20 h, there are two primary vortical remnants, seen as yellow circles, residing in O1 and O2. Both the vortical remnants and the Ψ-LCSs found at 20 h can be tracked and are still present at 30 h. The Ψ-LCSs travel with the vortices and separate them from turbulence. Many turbulent regions can be seen by repelling FTLE tangles in Fig. 10. These regions either split or merge, but do not leave behind vortical remnants.

4.8 Formation of primary eyewall

By 30 h, the turbulence above the boundary layer has decreased, and some repelling Ψ-LCSs emerge at the bottom of the boundary layer. The primary structures associated with O1 and O2 at 30 h are shown in Fig. 12a at $z = 40$ m. The vortical remnants are called V1 and V2, and the LCSs are labeled AL1, AL2, and RL1. AL1 and AL2 are attracting while RL1 is repelling. These particular vortical remnants are the primary vortices that are stretched into a ring of vorticity, while the Ψ-LCSs form the primary eyewall.

ACPD
11, 1–44, 2011

The evolution of the primary structures can be seen in Figu. 12b–d at 35 h, 40 h, and 45 h, respectively. AL1 and RL1 remain with V1 until 40 h, and prohibit the merger of V1 with other vortices. V1 is eventually stretched and becomes part of the primary eyewall by 45 h, after RL1 disappears. V2 is accompanied by AL2, and has no repelling LCS at 30 h. Over the next 15 h, AL2 stretches V2, and is a focal point for the attraction of high θ_e. As V2 stretches, it maintains high θ_e and forms the primary ring of vorticity at 45 h. AL2 stretches alongside V2, and forms the Lagrangian eyewall by 41 h, 4 h before the ring of vorticity is enclosed.

5 Conclusions

Using 3-D Lagrangian fields, we have examined 3-D structural aspects of tropical cyclone intensification using an idealized numerical experiment from prior work. Though the vertical motion associated with convection within VHTs provides a challenging setting for understanding mixing, the LCSs from our kinematically derived fields are able to isolate the individual VHT contributions. A series of conceptual models for binary vortex interaction in a planar flow help illustrate the role of LCSs near vortices, and the interaction described in the models is shown to persist and can be tracked through turbulent flow. Turbulent and organized flow regimes provided a comparison of the LCS structure near convectively active VHTs versus the persistent vortical remnants. The LCSs were shown to complement the system-scale inflow of the boundary layer by highlighting pathways for the stirring of θ_e and vorticity along attracting LCSs. Above the boundary layer, where the mean inflow is not as dominant, repelling LCSs emerged in conjunction with attracting LCSs to form pathways for stirring the vortical remnants and boundaries to protect them from the resolved turbulence. The LCSs showed vertical coherence along with the vortices, and convection was marked by a tangle of repelling LCSs. The influence of the localized LCSs concludes with the formation of the primary eyewall, as the preferred vortical remnants and the LCSs which travel with them are stretched into a ring of vorticity and an enclosed attracting LCS.

ACPD
11, 1–44, 2011

Though this study has been conducted using model data calculated from an idealized initialization which represents one member of an ensemble, our 3-D Lagrangian methods resulted in 3-D continuous LCSs persisting over varying initial time, and should provide similar results for any of the ensemble members associated with small perturbations in boundary layer moisture as described in Nguyen et al. (2008). The Lagrangian methods used in this study are applicable to a variety of time-dependent vortex flows from small scale turbulence to the system-scale circulation. Vortex behavior on these differing spatial scales can be studied by changing the integration time of the Lagrangian fields. These methods may uncover important localized aspects of transport that have been unattainable by other methods such as eddy statistics. Investigation of the role of Lagrangian coherent structures during hurricane genesis will be the goal of a future study.

Acknowledgements. This work was supported by the National Science Foundation under NSF Cooperative Agreement ATM-0715426. The authors thank Wayne Schubert, Michael Kirby, John Persing, and Michael Riemer for their discussions.

References

Bell, M. and Montgomery, M. T.: Sheared deep vortical convection in pre-depression Hagupit during TCS08, Geophys. Res. Lett., 37, L06802, doi:10.1029/2009GL042313, 2010. 3

Bolton, D.: The computation of equivalent potential temperature, Mon. Weather Rev., 108, 1046–1053, 1980. 4

Bui, H. H., Smith, R. K., Montgomery, M. T., and Peng, J.: Balanced and unbalanced aspects of tropical cyclone intensification, Quart. J. Roy. Meteor. Soc., 135, 1715–1731, 2009. 5, 17

Chen, Y. and Yau, M. K.: Asymmetric structures in a simulated landfalling hurricane, J. Atmos. Sci., 60, 2294–2312, 2003. 17

Dudhia, J.: A non-hydrostatic version of the penn state-ncar mesoscale model: Validation tests and simulation of an atlantic cyclone and cold front. Mon. Weather Rev., 8:1493–1513, 1993. 17

Dunkerton, T. J., Montgomery, M. T., and Wang, Z.: Tropical cyclogenesis in a tropical wave

ACPD

11, 1–44, 2011

critical layer: easterly waves, Atmos. Chem. Phys., 9, 5587–5646, doi:10.5194/acp-9-5587-2009, 2009. 3
Emanuel, K. A., Neelin, J. D., and Bretherton, C. S.: On large scale circulations in convecting atmosphere, Q. J. R. Meteorol. Soc., 120, 1111–1143, 1994. 4
Fang, J. and Zhang, F.: Initial development and genesis of Hurricane Dolly (2008), J. Atmos. Sci., 67, 655–672, 2010. 5
Grell, G., Dudhia, J., and Stauffer, D.: A description of the fifth generation Penn State-NCAR Mesoscale Model (MM5), NCAR Tech. Note NCAR/TN, 398, 1–138, 1995. 17
Haller, G.: Finding finite-time invariant manifolds in two-dimensional velocity fields, Chaos, 10, 99–108, 2000. 9
Haller, G.: Lagrangian coherent structures from approximate velocity data, Phys. Fluids, 14, 1851–1861, 2002. 9, 11
Haller, G. and Iacono, R.: Stretching, alignment, and shear in slowly varying velocity fields, Phys. Rev. E, 68, 056304–1–6, doi:10.1103/PhysRevE.08.056304, 2003. 9
Haller, G. and Poje, A.: Finite time transport in aperiodic flows, Physica D, 119, 352–380, 1997. 9
Haller, G. and Yuan, G.: Lagrangian coherent structures and mixing in two-dimensional turbulence, Physica D, 147, 352–370, 2000. 8, 9, 11
Hendricks, E. A., Montgomery, M. T., and Davis, C. A.: On the role of vortical hot towers in tropical cyclone formation, J. Atmos. Sci., 61, 1209–1232, 2004. 3, 5
Holton, J. R.: An introduction to dynamic meteorology, 4th Edn., Elsevier, 2004. 4, 5, 6
Ide, K., Small, D., and Wiggins, S.: Distinguished hyperbolic trajectories in time-dependent fluid flows: analytical and computational approach for velocity fields defined as data sets, Nonlin. Processes Geophys., 9, 237–263, doi:10.5194/npg-9-237-2002, 2002. 7, 23
Levina, G. and Montgomery, M. T.: A first examination of the helical nature of tropical cyclogenesis, Doklady Earth Sci., 434, Part I, 1285–1289, 2010. 5, 6
Lilly, D. K.: On the theory of disturbances in a conditionally unstable atmosphere, Mon. Weather Rev., 88, 1–17, 1960. 4
Malhotra, N. and Wiggins, S.: Geometric structures, lobe dynamics, and lagrangian transport in flows with aperiodic time-dependence, with applications to Rossby wave flow, J. Nonlinear Sci., 8, 401–456, 1999. 7
Melander, N. J., Zabusky, M. V. and McWilliams, J. C.: Symmetric vortex merger in two dimensions – causes and conditions, J. Fluid Mech., 195, 303–340, 1988. 25

ACPD
11, 1–44, 2011

Montgomery, M. T., Nguyen, V. S., Smith, R. K., and Persing, J.: Do tropical cyclones intensify by WISHE?, Q. J. R. Meteorol. Soc., 135, 1697–1714, 2009. 17, 19
Montgomery, M. T., Nichols, M. E., Cram, T. A., and Saunders, A. B.: A vortical hot tower route to tropical cyclogenesis, J. Atmos. Sci., 63, 355–386, 2006. 5, 10
Montgomery, M. T., Wang, Z., and Dunkerton, T. J.: Coarse, intermediate and high resolution numerical simulations of the transition of a tropical wave critical layer to a tropical storm, Atmos. Chem. Phys., 10, 10803–10827, doi:10.5194/acp-10-10803-2010, 2010. 5
Montgomery, M. T. and Smith, R. K.: Paradigms for tropical-cyclone intensification, Quart. J. Roy. Meteor. Soc., 137, 1–31, 2011. 5, 6
Nguyen, C. M., Reeder, M. J., Davidson, N. E., Smith, R. K., and Montgomery, M. T.: Inner-core vacillation cycles during the rapid intensification of Hurricane Katrina, Quart. J. Roy. Meteor. Soc., 137, 829–844, 2010. 4, 5, 19
Nguyen, S. A., Smith, R. K., and Montgomery, M. T.: Tropical-cyclone intensification and predictability in three dimensions, Q. J. R. Meterol. Soc., 134, 563–582, 2008. 5, 10, 17, 29
Prieto, R., McNoldy, B. D., Fulton, S. R., and Schubert, W. H.: A classification of binary tropical-cyclone-like vortex interactions, Mon. Weather Rev., 131, 2656–2666, 2003. 10
Provenzale, A.: Transport by coherent barotropic vortices. Ann. Rev. Fluid Mech., 31, 55–93, 1999. 10
Raymond, D. J. and López Carrillo, C.: The vorticity budget of developing typhoon Nuri (2008), Atmos. Chem. Phys., 11, 147–163, doi:10.5194/acp-11-147-2011, 2011. 3
Reasor, P. D., Montgomery, M. T., and Bosart, L.: Mesoscale observations of the genesis of Hurricane Dolly (1996), J. Atmos. Sci., 62, 3151–3171, 2005. 3
Rutherford, B. and Dangelmayr, G.: A 3d Lagrangian hurricane eye-eyewall computation, Quart. J. Roy. Meteor. Soc., 136, 1931–1944, 2010. 9, 10, 11, 13, 16, 20, 23
Rutherford, B., Dangelmayr, G., Persing, J., Kirby, M., and Montgomery, M. T.: Lagrangian mixing in an axisymmetric hurricane model, Atmos. Chem. Phys., 10, 6777–6791, doi:10.5194/acp-10-6777-2010, 2010. 9
Rutherford, B., Dangelmayr, G., Persing, J., Schubert, W. H., and Montgomery, M. T.: Advective mixing in a nondivergent barotropic hurricane model, Atmos. Chem. Phys., 10, 475–497, doi:10.5194/acp-10-475-2010, 2010. 9, 12, 13, 21
Saffman, P. G.: Dynamics of vorticity, J. Fluid Mech., 106, 49–58, 1981. 10
Sapsis, T. and Haller, G.: Inertial particle dynamics in hurricanes, J. Atmos. Sci., 66, 2481–2492, 2009. 9

ACPD
11, 1–44, 2011

Schubert, W. H. and Hack, J. J.: Inertial stability and tropical cyclone development, J. Atmos. Sci., 39, 1687–1697, 1982. 5
Shadden, S.: A dynamical systems approach to unsteady flows, PhD thesis, California Institute of Technology, 2006. 8
Shadden, S. C., Dabiri, J. O., and Marsden, J. E.: Lagrangian analysis of fluid transport in empirical vortex rings, Phys. Fluids, 18, 047105–1–11, doi:10.1063/1.2189885, 2006. 10
Shadden, S. C., Lekien, F., and Marsden, J. E.: Definition and properties of Lagrangian coherent structures from finite-time Lyapunov exponents in two-dimensional aperiodic flows, Physica D, 212, 271–304, 2005. 11
Shin, S. and Smith, R. K.: Tropical cyclone intensification and predictability in a minimal three-dimensional model, Q. J. R. Meteorol. Soc., 134, 1385–1395, 2008. 5, 10
Siggia, E.: High Raleigh number convection, Annu. Rev. Fluid Mech., 26, 137–168, 1994. 4
Sippel, J. A., Nielsen-Gammon, J. W., and Allen, S. E.: The multiple- vortex nature of tropical cyclogenesis, Mon. Weather Rev., 134, 1796–1814, 2006. 3
Smith, R. K., Montgomery, M. T., and Nguyen, V. S.: Tropical cyclone spin up revisited, Q. J. R. Meteorol. Soc., 134, 1385–1395, 2009. 5, 6
Smith, R. K., Montgomery, M. T., and Vogl, S.: A critique of Emanuel's hurricane model and potential intensity theory, Q. J. R. Meteorol. Soc., 134, 551–561, 2008. 17
Tang, W., Mathur, M., Haller, G., Hahn, D., and Ruggiero, F.: Lagrangian coherent structures near a subtropical jet stream, J. Atmos. Sci., 67, 2307–2319, 2010. 9
Truesdell, C.: The kinematics of vorticity, Indiana Uiversity Press, 1954. 10
Wang, Y.: Vortex rossby waves in a numerically simulated tropical cyclone, part ii: The role in tropical cyclone structure and intensity changes, J. Atmos. Sci., 59, 1239–1262, 2000. 17
Weiss, J. B. and Provenzale, A.: Transport and mixing in geophysical flows, Springer, 2008. 7
Wiggins, S.: The dynamical systems approach to Lagrangian transport in oceanic flows, Ann. Rev. Fluid Mech., 37. 295–328, 2005. 8
Willoughby, H. E.: Forced secondary circulations in hurricanes, J. Geophys. Res., 84, 3173–3183, 1979. 5

ACPD
11, 1–44, 2011

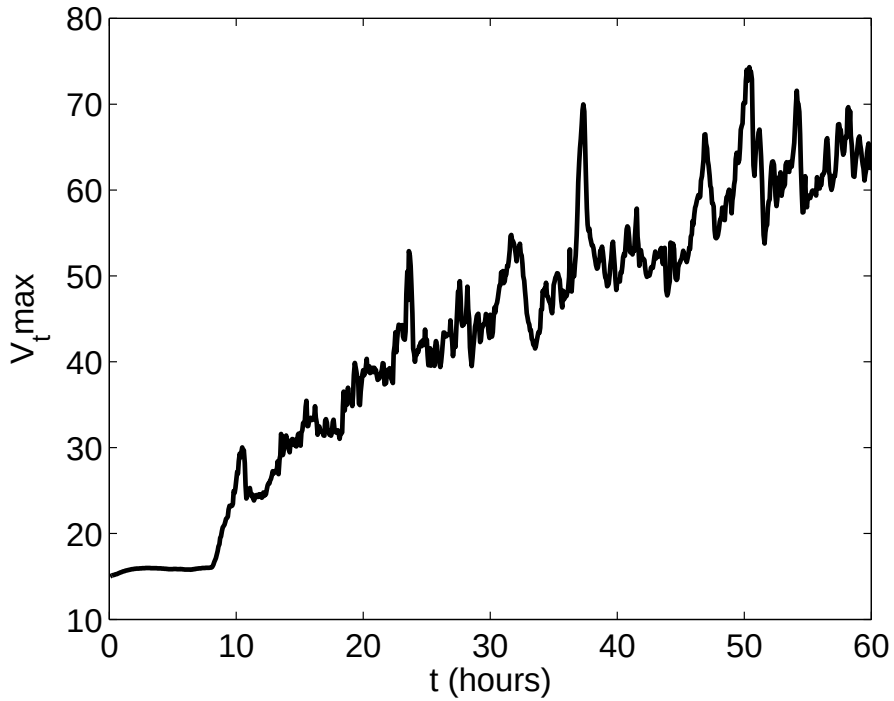

Fig. 1. Intensification of the simulated vortex is shown by the local maximum of horizontal wind speed V_t max as a function of time from $t = 0$ to $t = 60$ h.

ACPD
11, 1–44, 2011

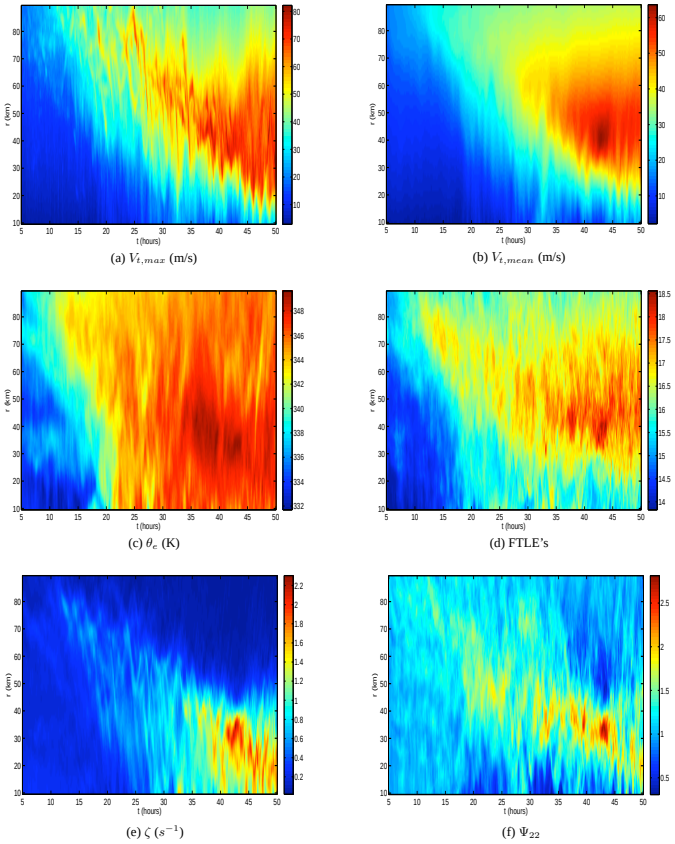

Fig. 2. Hovmoller plots (radial profile versus time) of azimuthally averaged $V_{\text{tan,max}}$ **(a)**, $V_{\text{tan,mean}}$ **(b)**, θ_e **(c)**, FTLE's **(d)**, ζ **(e)**, and Ψ_{22} **(f)**. The $V_{\text{tan,mean}}$, FTLE, Ψ_{22}, θ_e, and ζ values are averaged over the $z = 40$ m horizontal plane, while $V_{\text{tan,max}}$ is a maximum over all heights and azimuths at each radius.

ACPD
11, 1–44, 2011

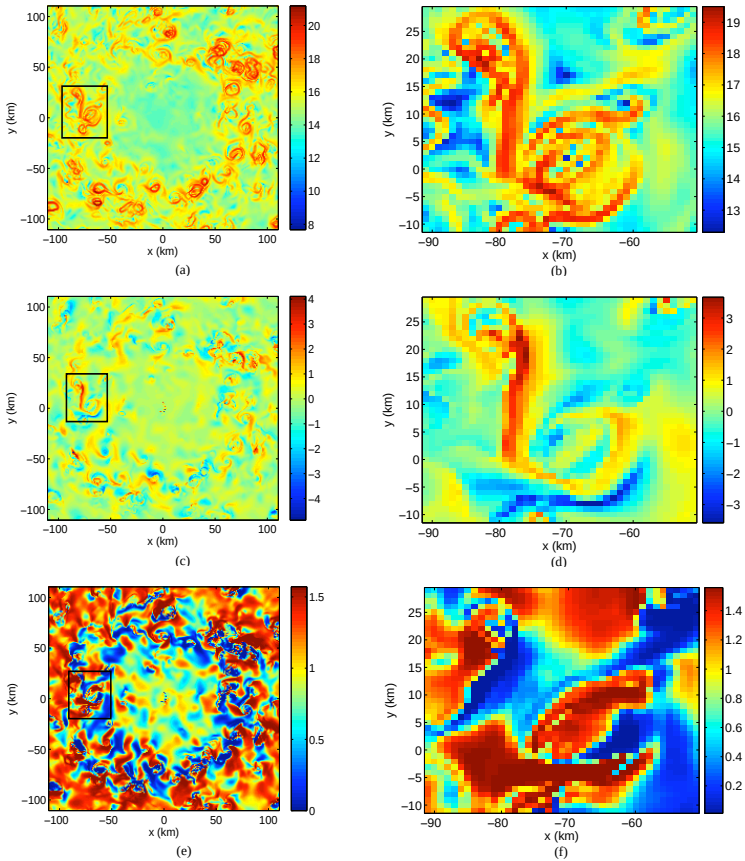

Fig. 3. Planar FTLE, Ψ_{22}, and φ fields in **(a)**, **(c)**, and **(e)**, respectively, at initial time of 10 h with integration time of 1 h at 1 km height. A zoom into a particular structure from the boxes in **(a)**, **(c)**, and **(e)** are shown in **(b)**, **(d)**, and **(f)**.

ACPD
11, 1–44, 2011

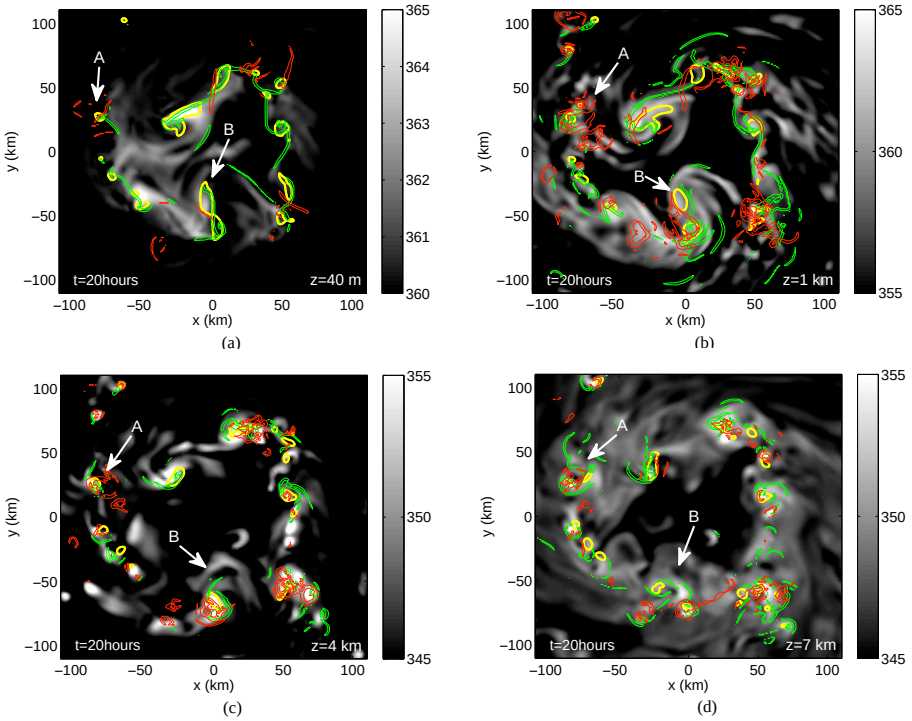

Fig. 4. The vertical structure of the LCSs are shown by attracting Ψ-LCSs (green) and repelling Ψ-LCSs (red), which with vorticity contours (yellow) are all overlaid on the θ_e field (black and white shading) at vertical levels of 40 m **(a)**, 1 km **(b)**, 4 km **(c)**, and 7 km **(d)**.

ACPD
11, 1–44, 2011

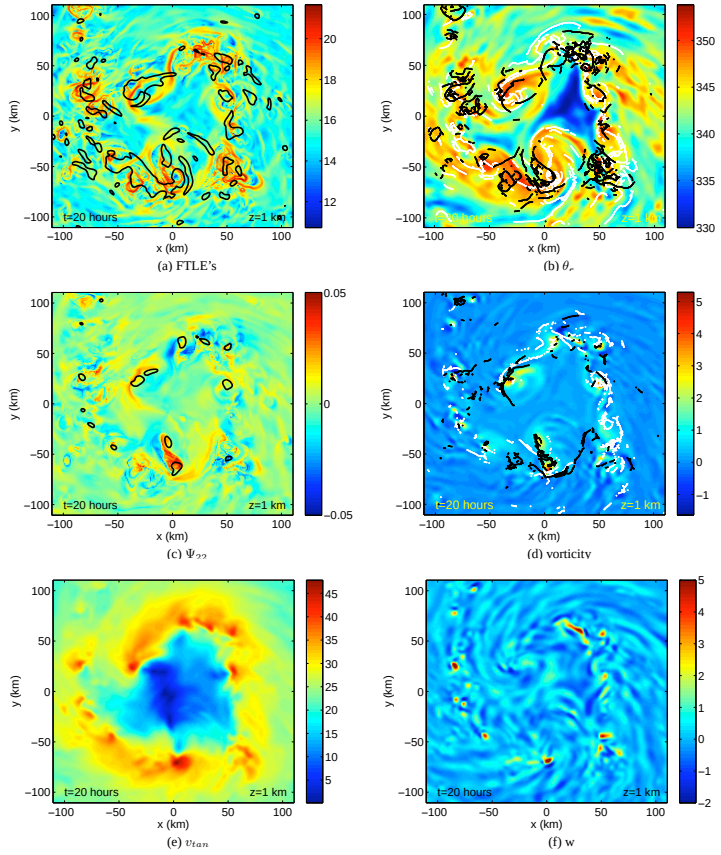

Fig. 5. Horizontal slices of Lagrangian fields and Eulerian diagnostics are compared at 20 h and 1 km height. The FTLE field **(a)** has ridges, which are extracted and overlaid on the θ_e field **(b)**. The Ψ_{22} field **(c)** has ridges, which are extracted and overlaid on the ζ field **(d)**. Tangential winds and vertical velocity are shown in **(e)** and **(f)**.

ACPD
11, 1–44, 2011

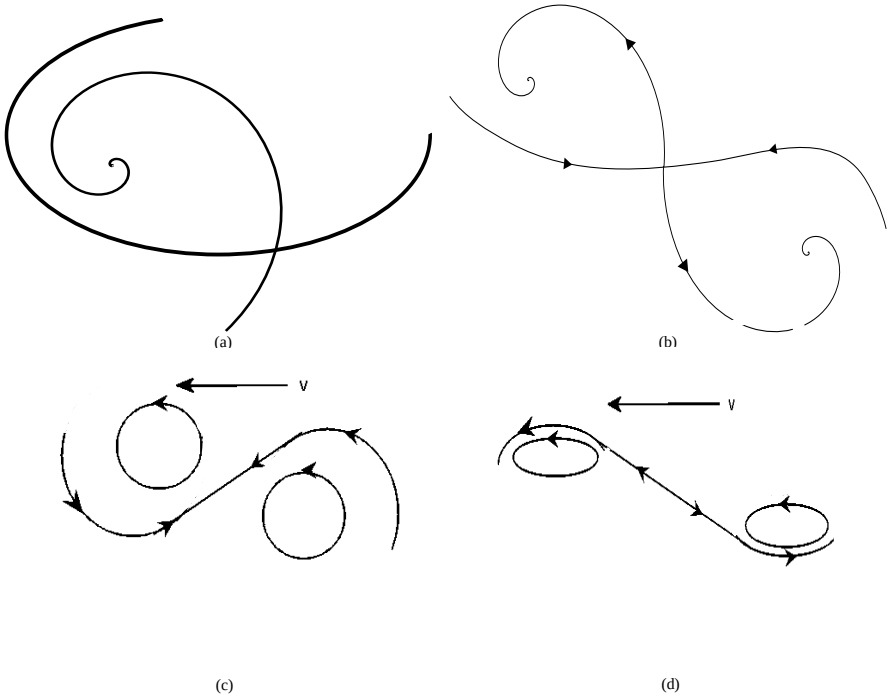

Fig. 6. The general saddle point geometry ocurrs when stable and unstable manifolds form a single convergent vortex **(a)**. A pair of convergent vortices on opposing sides of a saddle are kept from finite-time interaction **(b)**. Stable **(c)** and unstable **(d)** vortex interactions occur along a single manifold segment when the other manifold branch is not obtained under short integration times.

ACPD
11, 1–44, 2011

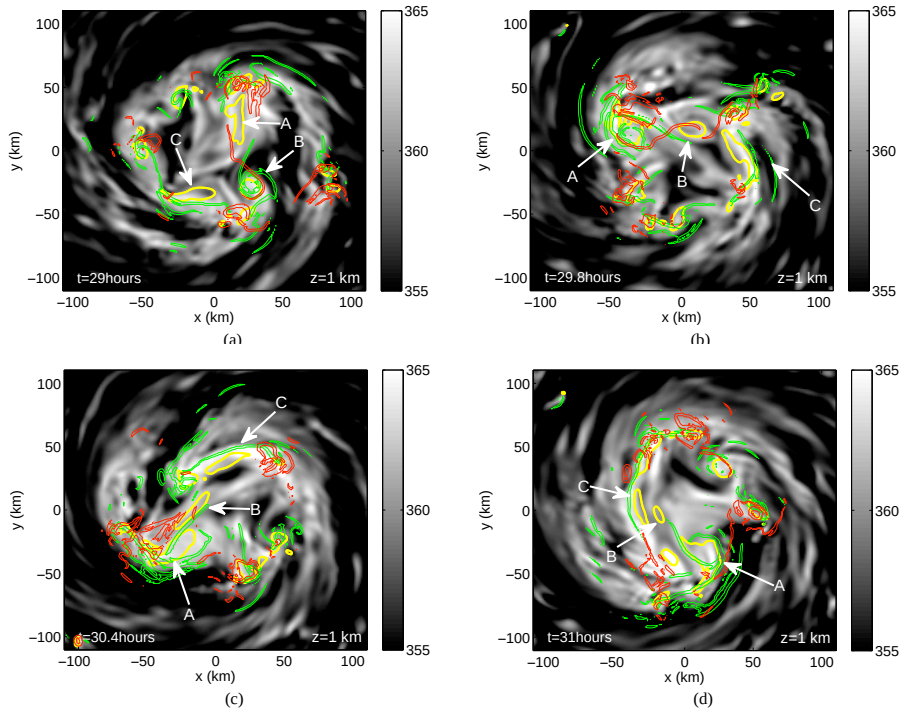

Fig. 7. An example of vortex interaction during the simulated intensification process. The times shown are 29 h **(a)**, 29.8 h **(b)**, 30.4 h **(c)**, and 31 h **(d)**. The yellow contours outline intense cyclonic vorticity anomalies whose values exceed $3 \times 10^{-3}\,s^{-1}$. Arrows point to a subset of interacting vortices discussed in Sect. 4.2. The intense vorticity regions, attracting Ψ-LCSs (green), repelling Ψ-LCSs (red), and vorticity contours (yellow) are all overlaid on the θ_e field (black and white shading).

ACPD
11, 1–44, 2011

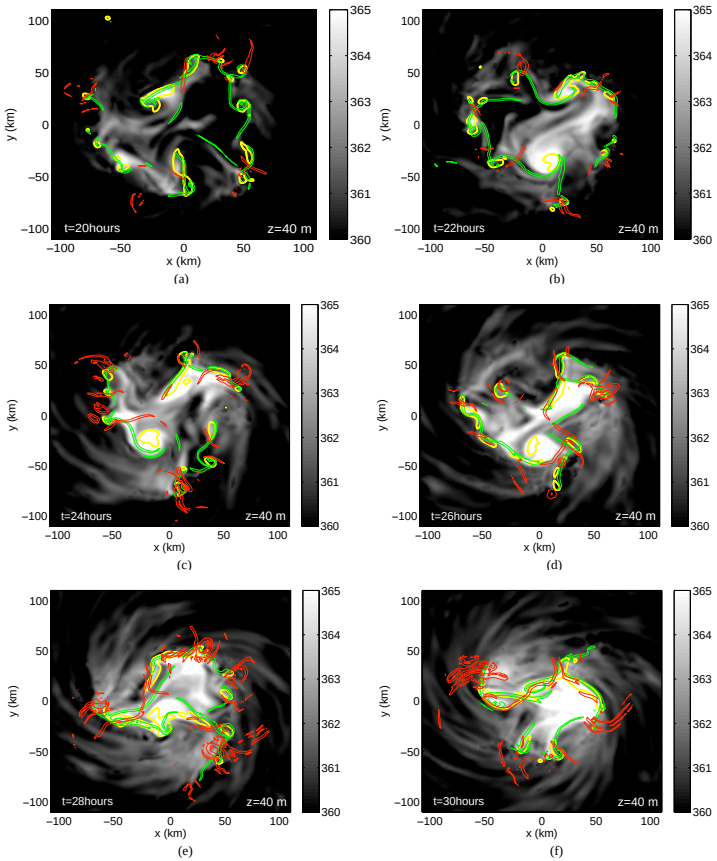

Fig. 8. Planar attracting (green) and repelling (red) FTLE ridges and vorticity contours (yellow) are overlaid on θ_e fields with 1 h integration time at times from 20 h to 30 h every 2 h at the bottom of the boundary layer.

ACPD
11, 1–44, 2011

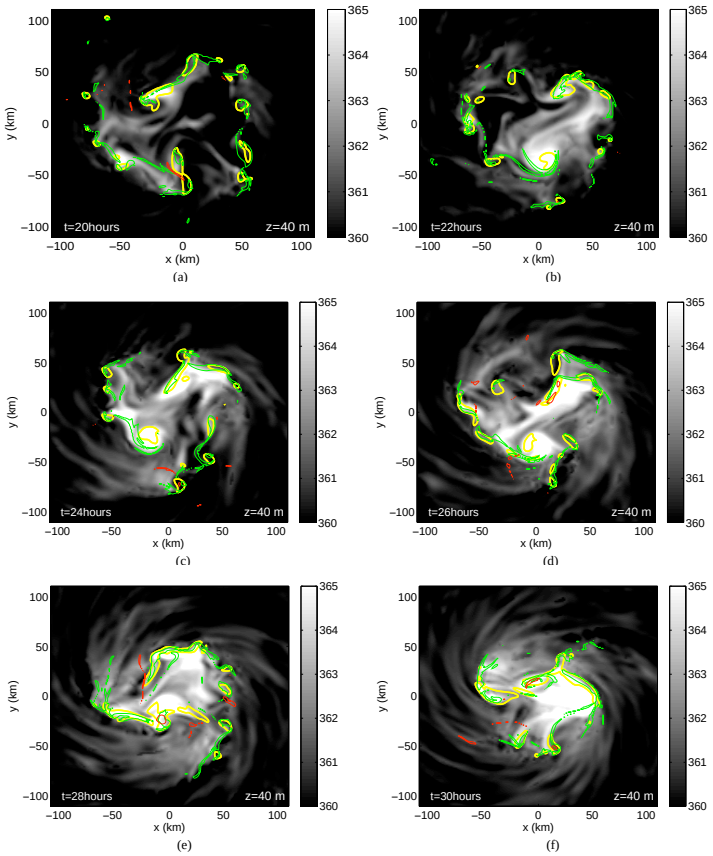

Fig. 9. Attracting (green) and repelling (red) Ψ_{22} ridges and vorticity contours (yellow) are overlaid on θ_e fields with 1 h integration time at times from 20 h to 30 h every 2 h at the bottom of the boundary layer.

ACPD
11, 1–44, 2011

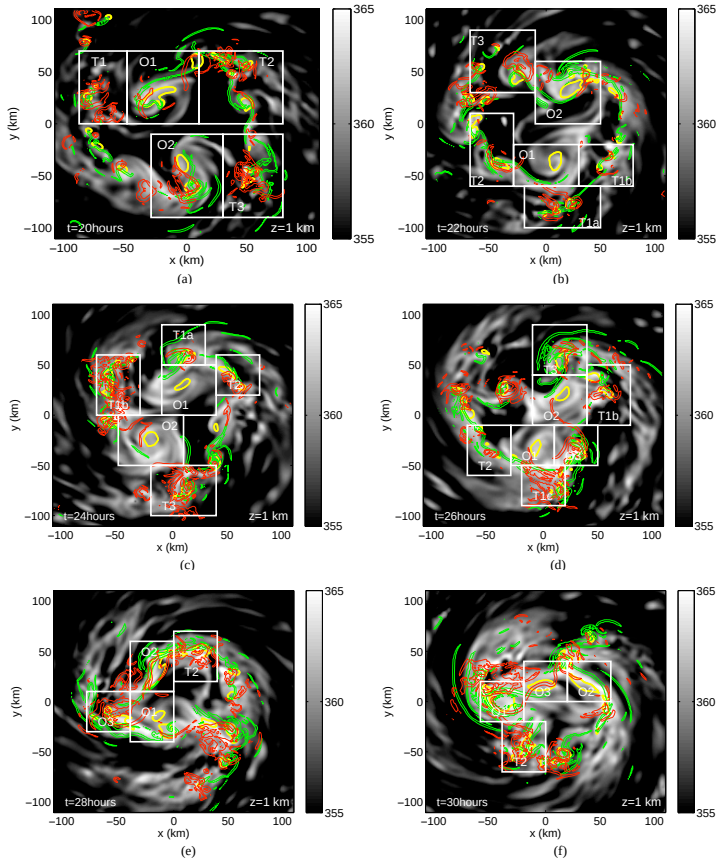

Fig. 10. Mixing regimes can be seen in labeled boxes containing FTLE LCSs at $z = 1$ km with 1 h integration time at times from 20 h to 30 h every 2 h. The attracting LCSs (green), repelling LCSs (red), and vorticity contours (yellow) are all overlaid on the θ_e field (black and white shading).

ACPD
11, 1–44, 2011

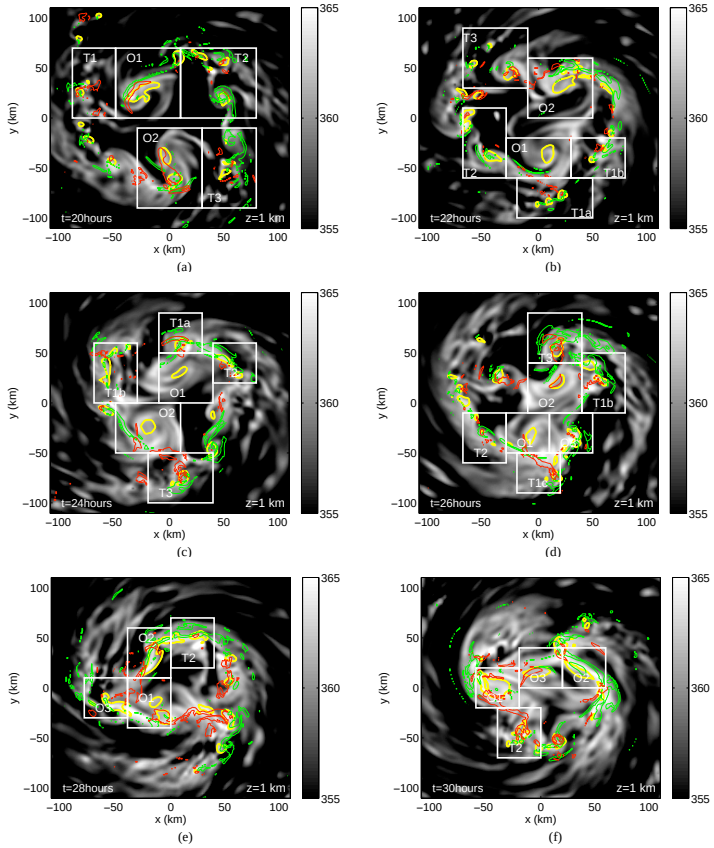

Fig. 11. Mixing regimes can be seen in labeled boxes containing Ψ_{22} LCSs at $z = 1$ km with 1 h integration time at times from 20 h to 30 h every 2 h. The attracting Ψ-LCSs (green), repelling Ψ-LCSs (red), and vorticity contours (yellow) are all overlaid on the θ_e field (black and white shading).

ACPD
11, 1–44, 2011

Lagrangian coherent structures in tropical cyclone intensification

B. Rutherford et al.

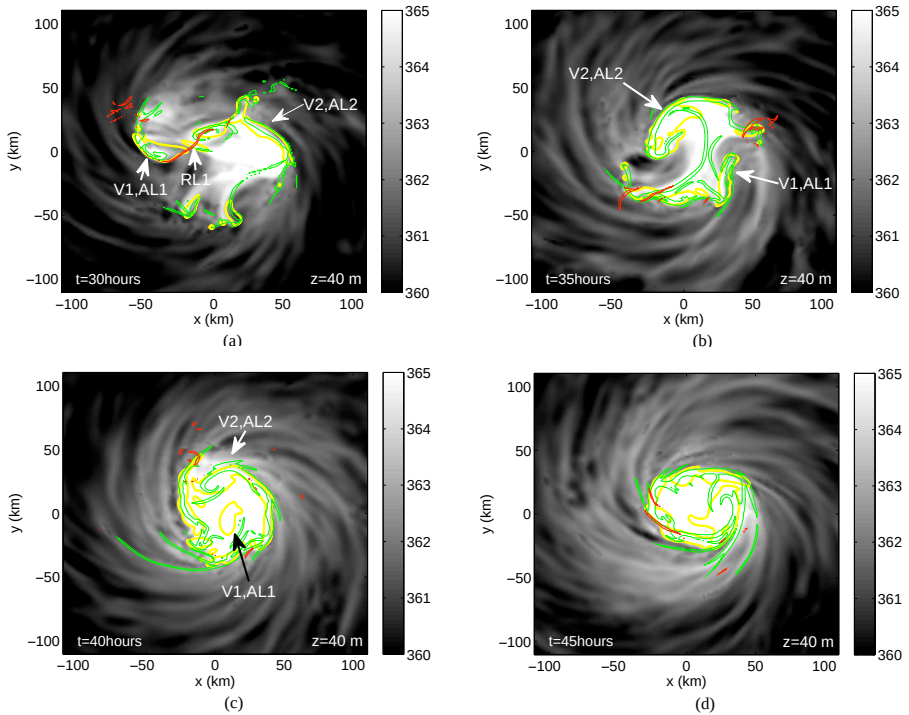

Fig. 12. The primary Lagrangian structures present during primary eyewall formation at the bottom of the boundary layer as described in Sect. 4.6 are labeled by arrows and are shown at 30 h **(a)**, 35 h **(b)**, 40 h **(c)**, and 45 h **(d)**. Attracting Ψ-LCSs (green), repelling Ψ-LCSs (red), and vorticity contours (yellow) are all overlaid on the θ_e field (black and white shading).

ACPD
11, 1–44, 2011